1 **Quantitative Study of Storm Surge Risk Assessment in Undeveloped Coastal Area of China**

2 **Based on Deep Learning and Geographic Information System (GIS) Techniques: A Case**

3 **Study of Double-Moon Bay Zone**

4 Lichen Yu [a, d], Shining Huang [c], Hao Qin [*, a, d], Wei Wei [a, d], Lin Mu [*, b]

5 [a] Hubei Key Laboratory of Marine Geological Resources, College of Marine Science and

6 Technology, China University of Geosciences, Wuhan, China, 430074

7 [b] College of Life Sciences and Oceanography, Shenzhen University, Shenzhen, China, 518060

8 [c] Marine Information Center, Department of Natural Resources of Huizhou Bureau, Huizhou,

9 China, 516003

10 [d] Shenzhen Research Institute, China University of Geosciences, Shenzhen, China, 518057

11

12 [*] Corresponding authors: Hao Qin (qh1qh100@alumni.sjtu.edu.cn); Lin Mu (moulin1977@h

13 otmail.com).

14

15 **Abstract**

16 Storm surge is a common nature disaster in China southern coastal area, which usually causes

17 heavy human life and economic losses. With the economic development and population

18 concentration of coastal cities, the storm surges may result in more impacts and damage in the

19 future. Therefore, it is of vital importance to conduct risk assessment to identify high-risk areas

20 and evaluate economic losses. However, quantitative study of storm surge risk assessment in

21 undeveloped areas of China is difficult, since there is a lack of building characters and damage

22 assessment data. Aiming at the problem of data missing in undeveloped areas of China, this paper

23 proposes a methodology for conducting storm surge risk assessment quantitatively based on deep

24 learning and geographic information system (GIS) techniques. Five defined storm surge

25 inundation scenarios with different typhoon return periods are simulated by coupled

26 FVCOM-SWAN model, the reliability of which is validated using official measurements. Building

27 footprints of the study area are extracted through TransUNet deep learning model and Remote

28 Sensing Image (RSI), while building heights are obtained through Unmanned Aerial Vehicle (UAV)

29 measurement. Subsequently, economic losses are quantitatively calculated by combing the

30 adjusted depth-damage functions and overlay analysis of the buildings exposed to storm surge

31 inundation. Zonation maps of the study area are illustrated to display the risk levels according to

32 the economic losses. The quantitative risk assessment and zonation maps can help the government

33 to make storm surge disaster prevention measures and optimize land use planning, and thus to

34 reduce the potential economic losses of the coastal area.

35

36 **Keywords:** Strom surge; Quantitative risk assessment; GIS; Deep learning; Risk zonation map

37

38 **1. Introduction**

39   Storm surge, defined as the abnormal rise of water over and above the normal astronomical

40 tide, and is expressed in terms of height above predicted or expected tide levels. Mostly, the surge

41 is generated by a strong atmospheric disturbance, and it becomes particularly catastrophic when it

42 happens to coincide with an astronomical high tide. In that case, the surge-driven coastal flooding

43 may inundate buildings and cropland, cause significant casualties and economic losses. Storm

44 surges have caused widespread damage worldwide. In 2013, super typhoon Yolanda as the worst

45 typhoon in last 30 years, pounded the Philippines. It caused 6293 individuals reported dead, 28689
46 injuries and 1061 individuals missing, with estimated damages totaling 864 million US dollars
47 (Mcpherson, 2015). Hurricane Harvey struck Texas in August 2017, resulting in approximately
48 100 deaths and economic losses exceeding 125 billion dollars (Lee, 2021). In China, storm surges
49 also pose a frequent threat in the coastal cities. In the last decade, China has experienced an
50 average of 8.5 storm surge disasters annually, with an average damage amount of 6815.8 million
51 yuan per year, where Guangdong and Zhejiang Provinces are the most affected coastal areas
52 (China Marine disaster bulletin, 2022). For example, Typhoon Hato in 2017, Typhoon Mangkhut
53 in 2018, Typhoon Lekima in 2019 has caused significant damage to coastal cities in China, and
54 resulted great losses of life and property. For the past few years, as the rapid development of
55 population and economic in China coastal area, the potential monetary loss grows accordingly
56 (Fang et al., 2021; Ji et al., 2020; Mcgranahan et al., 2007; Seto et al., 2011). Therefore, it is
57 crucial to implement risk assessment and mapping strategies to effectively reduce these risks and
58 mitigate the impact of storm surges.

59   Storm surge hazard assessment is an essential component of storm surge risk assessment and
60 zoning, aiming to evaluate the hazard intensity of disasters, through numerical simulation of storm
61 surge processes, estimation of storm surge for selected return periods, and computation of the
62 probable maximum storm surge (Shi et al., 2013). Therefore, the numerical simulation of storm
63 surge is a key step for storm surge risk assessment. However, because of the limitation of
64 historical storms and the nondeterminacy of future storm, numerical simulation of storm surges is
65 usually used to determine storm levels. Advanced Circulation Mode (ADCIRC) is a widely used
66 hydrodynamic model in coastal area. For example, Vijayan et al. (2021) utilized ADCIRC model
67 to simulate storm surges and tides during the hurricane that land on Florida in 2018, for the
68 purpose of comparing the different impact of wind model Holland 1980 and Holland 2010. Wang
69 et al. (2021a) and Liu and Huang (2020) used ADCIRC and Simulating Waves Nearshore (SWAN)
70 coupled model respectively simulate the storm surge and wave in the sea near Shandong Peninsula
71 and Taiwan, and the hazard assessment and model verification were carried out respectively.
72 Delft3D is a comprehensive numerical modeling system for simulating hydrodynamic processes.
73 Hu et al. (2022) adapted a pre-validated Delft3D-based hydrodynamic model proved the impact of
74 levee opening at selected locations was minor. Lyddon et al. (2019) used Delft3D-FLOW-WAVE
75 model calculate the tide and wave in the Severn Estuary, the result pointed out the importance of
76 locally generating winds in simulation of water level and wave height. Finite Volume Coastal
77 Ocean Model (FVCOM) is another widely used numerical model for simulating hydrodynamic
78 processes. Zhang et al. (2020) conducted a series of modeling experiments with the purpose of
79 assessing the impact of storm and evaluated the flood protection by using FVCOM inundation
80 model. Zhu et al. (2022) realized WRF-SWAN-FVCOM coupling simulation to analyze the
81 spatial-temporal evolution laws, and the result demonstrate the method can predict hydroelastic
82 responses of the maritime airport under the impact of typhoons, currents and waves.

83   It has been demonstrated that it is critical to include tide and sea-water-level variations in
84 shelf and nearshore wave simulations (Masson, 1996). Furthermore, the sea water level could be
85 significantly affected by strong tide and typhoon-induced wind in complex coastal seas and then
86 modulate the wave properties (Yang et al., 2020). Coupled FVCOM-SWAN model, with the
87 foundation of FVCOM's finite volume method, unstructured grid, and adaptable boundary
88 condition handling capability, integrating the hydrodynamic and wave processes of SWAN,

89 possesses the ability to provide simulation result more quickly and accurately. In this circumstance,
90 coupled FVCOM-SWAN model is used in this research for simulating the inundation of storm
91 surge.

92 Coastal risk assessment can be categorized into two primary classifications: qualitative and
93 quantitative. In the realm of qualitative assessment, entropy weight method, Analytic Hierarchy
94 Process (AHP) and other methods are widely used. Ramkar and Yadav (2021) used AHP in
95 combination with Geographic Information Systems (GIS) for proposing a flood risk map, which
96 can identify the high-risk areas efficiently. Malekinezhad et al. (2021) combined the entropy
97 weight method and GIS, and conducted a flood vulnerability analysis for Hamadan city. The result
98 highlighted the advantages of entropy weight method comparing to normal spatial overlay method.
99 Besides, Pathan et al. (2022) and Rafiei-Sardooi et al. (2021) made use of Technique for Order
100 Preference of Similarity by Ideal Solution (TOPSIS). The former pointed out the advancement of
101 TOPSIS by comparing with AHP, and the latter combined machine learning and TOPSIS to
102 analyze urban flood vulnerability. Unlike qualitative risk assessment, quantitative risk assessment
103 enables the quantification of damages and risks in monetary terms. The most commonly used
104 approach to assess direct damages is based on depth-damage curves (De Moel and Aerts, 2011;
105 Merz et al., 2007; Smith, 1994). Thieken et al. (2008) presented the Flood Loss Estimation Model
106 for the private sector (FLEMOps) through using the Germany flood losses data in August 2002,
107 and the group further established model for commercial sector in 2010 (Kreibich et al., 2010).
108 Zhai et al. (2005) derived multi-factor loss functions for buildings in Nagoya, Japan using
109 empirical data from Tokai flood in 2000, and Grahn and Nyberg (2014) established functional
110 relationships utilizing the house insurance claims data caused by lake flooding. Except for
111 buildings, Yazdi and Salehi Neyshabouri (2012) and Hess and Morris (1988) respectively built
112 several uni-variable functions and multi-factor functions for kinds of crops and grassland. In
113 recent years, machine learning is also introduced in quantitative loss assessment, for example,
114 Merz et al. (2013) developed a tree-based approach using Regression Tree and Bagging
115 Regression Tree as machine-learning methods to analysis of direct building damage to private
116 homes. Paprotny et al. (2020) proposed a Bayesian Network damage model (a
117 Supervised-Machine-Learning method), and reached a good accuracy of predictions of building
118 losses.

119 The essence of quantitative risk assessment lies in analyzing the interaction between
120 exposure factors and hazards (Adnan et al., 2020; Armenakis and Nirupama, 2013; Granger, 2003;
121 Kron, 2005), therefore it's crucial to quantify the direct tangible damage of elements at risk.
122 Buildings are important exposure elements, as they are the gathering place of population and
123 property. Building footprint data is necessary for evaluating the vulnerabilities of a building, as it
124 provides essential information about the buildings, including spatial location, distribution, and
125 boundaries and so on (Mharzi Alaoui et al., 2022). It's also of great significance in risk assessment,
126 primarily due to its ability to identify high-risk areas, assess building vulnerability and estimate
127 potential damage (Gacu et al., 2023; Wu et al., 2019). Extracting building footprints from remote
128 sensing images has been widely used in many fields. For example, in urban planning, Zhou et al.
129 (2004) used building footprint data and LiDAR point cloud data for urban 3D modeling; Tang et al.
130 (2006) proposed a GIS-based landscape index combing with remote sensing to analyze urban
131 sprawl spatial fragmentation. In disaster management, Liu et al. respectively evaluated seismic
132 vulnerability in Urumqi and Weinan in China (Liu et al., 2019; Liu et al., 2020). In navigation,

133 Rousell and Zipf (2017) proposed a prototype navigation service based on multi-index in OSM
134 dataset and building footprints, and Chen and Gao (2019) merged GPS pseudorange, LiDAR
135 odometry measurements and building footprint to offer a UAV navigation algorithms. However,
136 there is a lack of building footprints extraction and application in the realm of storm surge
137 assessment.

138   In view of the aforementioned information, regarding storm surge qualitative risk assessment,
139 there is a stringent requirement for both the quality and timeliness of land use data, which means
140 that the risk assessment cannot be generated in real time, and the qualitative risk assessment also
141 can't evaluate the risk level through the intuitive value of economic loss. In the realm of
142 quantitative risk assessment, building a uni-variable or multi-factor empirical model requires
143 complete and substantial data, and the published models generally only provide uni-variable
144 functions ignoring the building height as a factor, or have regional limitations. Additionally, for
145 the coastal regions of China, which are often affected by storm surge disasters, they tend to have
146 relatively low levels of economic development. Under the circumstances, the data needed to
147 conduct flood risk assessment is generally in a state of absence.

148   In response to the challenges mentioned above, the scientific goal of this paper is to propose a
149 quantitative storm surge risk assessment method for underdeveloped areas based on deep learning
150 and GIS techniques. First, on the basis of high-resolution DEM and seawall data measurement,
151 five defined storm surge inundation scenarios with different typhoon return periods are simulated
152 by employing the coupled FVCOM-SWAN model. Subsequently, TransUNet is introduced as a
153 deep learning method to extract building footprint, and building's height data is acquired through
154 UAV measurement. Since data on relevant disaster losses in underdeveloped regions are lacking,
155 empirical modeling was deemed impractical. Therefore, the adjustment of the JRC's
156 depth-damage curves by the HAZUS is chosen to take the impact building's height into
157 consideration, thus to conduct a quantitative assessment with more accuracy. Finally, combining
158 hazard map, exposure elements and adjusted depth-damage curves, the quantitative risk zoning
159 maps are conducted. The risk zoning maps can assist decision-makers in identifying high-risk
160 sub-zones and planning disaster prevention measures. Accordingly, the novelty can be seen in
161 obtaining refined exposure elements data through deep learning and UAV, addressing the lack of
162 historical storm surge economic loss data and considering the effect of building height on
163 economic loss through the adjustment of existing depth-damage curves.

164 **2. Study area and datasets**
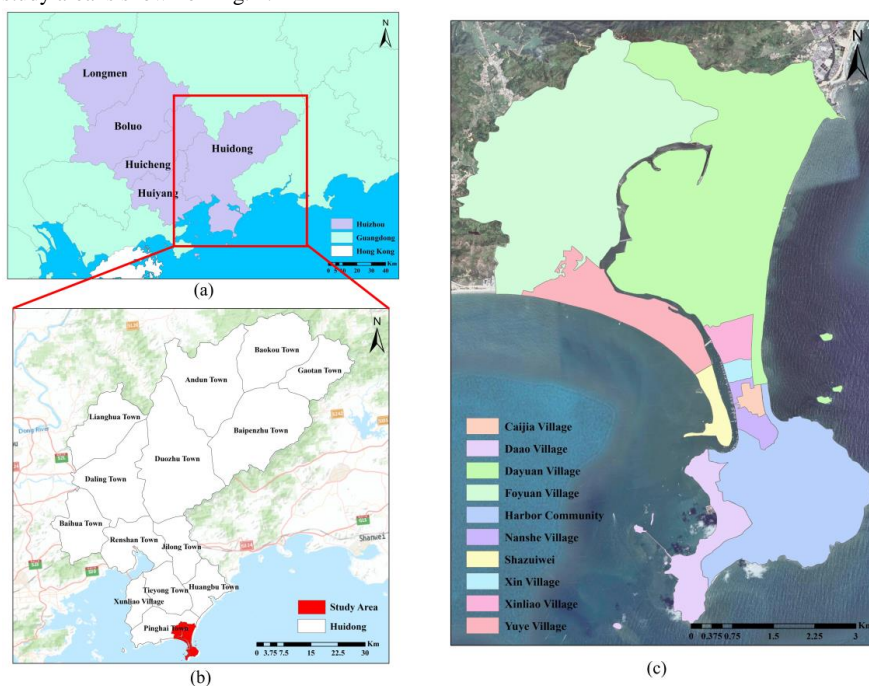
165 *2.1. Study area*

166   Being the shipping hub in the South China Sea, Guangdong province, located in southern
167 China, has become the largest economic province in China since 1989, with a GDP of 129118.6
168 billion yuan in 2022. Due to the seaborne trade, Guangdong has been the largest economic
169 province in China since 1989, which reached a GDP of 129118.6 billion yuan in 2022. However,
170 just as mentioned above, Guangdong is relatively vulnerable to storm surges because of its
171 geographical characteristics, such as Typhoon Hato and Typhoon Mangkhut.

172   Huizhou is one of the cities in Guangdong province, and also one of the central cities of Pearl
173 River Delta region. It's located at on the east coast of Guangdong-Hong Kong-Macao Greater Bay
174 Area, the GDP reached 540.1 billion yuan in 2022, with the highest growth rate in Guangdong.
175 Pinghai Town located at the southernmost of Huizhou, and has a registered population of about
176 forty thousand. Its economic source mainly depends on various crops and seafood products. Due

Natural Hazards
and Earth System
Sciences
Discussions

177   to its coastal geographical characteristics and the presence of Pinghai Ancient City, the town has
178   become a cultural tourist destination and can therefore be defined as a cultural tourist town.
179   In this paper, the chosen study region is the coastal area of Pinghai town, named the
180   Double-Moon Bay Zone. It covers ten villages in total, including Foyuan, Dayuan, Yuye, Xinliao,
181   Xin village, Shazuiwei, Cajia, Nanshe, Daao, and Harbor community. These years, the region has
182   been developed in tourism and real estate project development including construction of hotel,
183   resort, and high-end business district, which vastly prompt the financial development. It is
184   foreseeable that the population and economy of the region will growth rapidly. However, the
185   region's general economic status, which remains relatively low, and it consequently gives rise to
186   the challenge of data scarcity and limited accessibility. In addition, the region is susceptibly
187   affected by the tropical cyclones during the season running from April to November (Wang et al.,
188   2021b). Recent years, more than ten typhoons have affected the study area, including Typhoon
189   Lekima, Typhoon Haishen, Typhoon Kanuni etc. The general location and information about the
190   study area is shown on Fig. 1.

192   **Fig. 1.** The maps of locations in the study: (a) The map of Huizhou; (b) The map of study area in
193   Huidong, the base map is obtained from ESRI; (c) The village map of study area, the base map is
194   obtained from © GoogleMaps (map data © 2023 Google).

196   *2.2. Data source*
197   In order to accomplish the research, the data used is obtained from various sources, here is
198   the describe of different data:
199   (1) Land Cover Types data: the data is obtained from the Department of Natural Resources of
200   Huizhou Bureau. It contains multiple land cover types including forest, cropland, residential land,
201   etc. It is used to calculate vulnerability level.

202   (2) Remote sensing images: the remote sensing images are obtained from Chang Guang
203   Jilin-1 satellite. Chang Guang Satellite technology CO., LTD was founded on December 1st 2014,
204   which is the first and the largest commercial satellite corporation in China. Jilin-1 is the first
205   self-developed commercial high-resolution satellite. The images from Jilin-1 satellite have a
206   resolution of 50 cm, and have five spectral channels: Panchromatic band; Blue band; Red band;
207   Green band; Near Infrared band. The images consisting of blue band, red band, green band are
208   utilized to combine deep learning method, thus achieve the extraction of buildings.
209   (3) Unmanned Aerial Vehicle (UAV) data: the UAV data is generated by oblique photography,
210   and is organized by Open Scene Graph Binary format. The UAV data is obtained from Department
211   of Natural Resources of Huizhou Bureau, and the data is utilized for buildings' height calculation.
212   (4) Digital elevation model (DEM) data: the DEM data is captured by manual observation in
213   2018, with the resolution of 0.3m. The coordinate system and file organization are originally
214   CGCS 2000 and txt file, and further transformed to WGS 1984 and raster format to make use of
215   these data in the research. The data contains the elevation information for the study region.
216   Besides, the seawall data is also obtained manually. Both data are used in modeling of storm
217   surges for simulating the hazard maps.
218   (5) ERA5 data: ERA5 is the fifth generation of the European Reanalysis dataset produced by
219   the European Centre for Medium-Range Weather Forecasts (ECMWF), and it provides the
220   comprehensive and high-resolution atmospheric and climate data. In this study, the data is used in
221   conjunction with the Holland method to generate fused wind field data, which is subsequently
222   utilized for storm surge simulations.
223   (6) Historical typhoon data: the historical typhoon data including typhoon track, typhoon
224   pressure, and velocity are obtained through China Meteorological Administration Typhoon
225   Network Website. The historical data is employed to assess the reliability and validity of the
226   model.
227   (7) Administrative Boundary data: the data is obtained from National geographic information
228   public service platform, and it contains administrative boundaries at village level. There are ten
229   villages in the study area.
230
231   **3. Method**
232   The methods in this study aim to assess quantitative direct tangible damage over the study
233   area consists of following steps: hazard assessment; exposure assessment; vulnerability
234   assessment; risk assessment, and the flowchart of the procedure is illustrated in Fig. 2.
235   First, with respect to hazard assessment, five storm surge scenarios are defined. After
236   constructing wind field through Holland model, the inundation area and depth of different typhoon
237   return periods are simulated by utilizing the coupled FVCOM-SWAN model. In exposure
238   assessment, building footprints and heights are extracted by introducing a deep learning method
239   TransUNet and shadow calculation. Then the hazard maps are overlaid to identify the elements at
240   risk. Considering the effect of building's floor in flood monetary loss estimation, the JRC's
241   depth-damage functions are adapted representing the vulnerability of different exposed elements.
242   Eventually, the economic loss of different typhoon scenarios can be summarized and the risk
243   assessment is conducted through multiplying the temporal probability. Moreover, the quantitative
244   zoning maps of four risk levels are generated through zonal statistic.

Natural Hazards
and Earth System
Sciences
Discussions

245
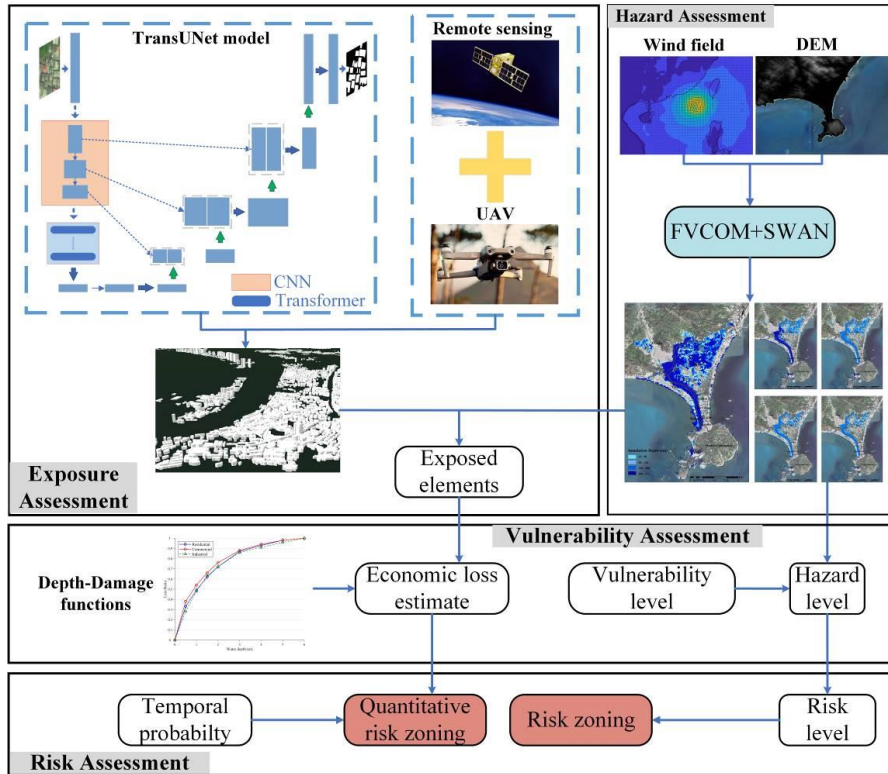
Fig. 2. The flowchart of the presented storm surge quantitative risk assessment method. The base
map is obtained from © GoogleMaps (map data © 2023 Google).

3.1. Strom surge inundation simulation

Finite Volume Coastal Ocean Model (FVCOM), is a coastal ocean circulation model, which
was originally developed by Chen et al. (2003), and further improved by the University of
Massachusetts and the Woods Hole Oceanographic Institution. The following are the governing
equations of FVCOM, comprising momentum, continuity, temperature, salinity, and density
equations:

$$\frac{\partial u}{\partial t} + u\frac{\partial u}{\partial x} + v\frac{\partial u}{\partial y} + wfv = -\frac{1}{\rho_o}\frac{\partial P}{\partial x} + \frac{\partial}{\partial z}\left(K_m\frac{\partial u}{\partial z}\right) + F_u \tag{3.1}$$

$$\frac{\partial v}{\partial t} + u\frac{\partial v}{\partial x} + v\frac{\partial v}{\partial y} + w\frac{\partial v}{\partial z} + fu = -\frac{1}{\rho_o}\frac{\partial P}{\partial y} + \frac{\partial}{\partial z}\left(K_m\frac{\partial v}{\partial z}\right) + F_v \tag{3.2}$$

$$\frac{\partial P}{\partial z} = -\rho g \tag{3.3}$$

$$\frac{\partial u}{\partial x} + \frac{\partial v}{\partial y} + \frac{\partial v}{\partial z} = 0 \tag{3.4}$$

$$\frac{\partial T}{\partial t} + u\frac{\partial T}{\partial x} + v\frac{\partial T}{\partial y} + w\frac{\partial T}{\partial z} = \frac{\partial}{\partial z}\left(K_h\frac{\partial T}{\partial z}\right) + F_T \tag{3.5}$$

Natural Hazards
and Earth System
Sciences

Discussions

$$\frac{\partial S}{\partial t} + u\frac{\partial S}{\partial x} + v\frac{\partial S}{\partial y} + w\frac{\partial S}{\partial z} = \frac{\partial}{\partial z}\left(K_h\frac{\partial S}{\partial z}\right) + F_S \tag{3.6}$$

$$\rho = \rho(T, S) \tag{3.7}$$

255 Where x, y and z respectively represent the east, north and vertical coordinate axes in the
256 Cartesian coordinate system; u, v and w are the velocity components in x, y,
257 z directions; T, S and ρ are the temperature, salinity and density; P is the pressure and
258 f stands for the Coriolis parameter; K_m is the vertical eddy viscosity coefficient and K_h is
259 the vertical eddy diffusivity coefficient for heat; g is the gravitational acceleration; F_u, F_v,
260 F_T, and F_S are the horizontal diffusion terms.

261 Simulating Waves Nearshore (SWAN) is the third-generation offshore wave model developed
262 by Delft University of Technology and it was originally proposed by Booij et al. (1996). The
263 governing equation of the model is shown as

$$\frac{\partial}{\partial t}N + \frac{\partial}{\partial x}C_x N + \frac{\partial}{\partial y}C_y N + \frac{\partial}{\partial \gamma}C_\gamma N + \frac{\partial}{\partial \theta}C_\theta N = \frac{S}{\gamma} \tag{3.8}$$

264 Where N is the wave action density; θ is the propagation direction; C_x, C_y are
265 respectively the x, y components of propagation speed and C_γ, C_θ are the γ,
266 θ components of propagation cospeed; γ and S respectively represent the frequency and the
267 source term for the wave energy.

268 FVCOM and SWAN both use the unstructured triangular grid to subdivide the South China
269 Sea, and the latitude and longitude range of the region is 13°N - 29°N, 109°E-122°E. The SWAN
270 parameters are set as follows: wind input growth term and whitecap dissipation term are the
271 Komen scheme; Bottom friction dissipation is parameterized using the Madsen vortex viscosity
272 model; The nonlinear interactions are implemented using three-wave and four-wave nonlinear
273 interaction schemes. The input wind field is the fusing wind field derived from ERA5 and the
274 Holland method. The open boundary forced tidal elevation of FVCOM is conducted by calculating
275 the harmonic constants for the eleven major astronomical tidal constituents, namely M2, N2, S2,
276 K2, K1, O1, P1, Q1, MS4, M4, and M6. The forcing field is the fusing wind field and the wave
277 data generated by SWAN. The external model time step for the model is set to 0.75 second, while
278 the internal model time step is set to 7 seconds.

279 In the present study, FVCOM-SWAN coupling method is utilized for simulating the
280 inundation caused by storm surge. Specifically, following the modification of typhoon Mangkhut's
281 central pressure, velocity, and track data, the data is utilized as input for the Holland typhoon wind
282 field model, subsequently yielding the wind field outcome. The wind field data extracted is fed
283 into the SWAN model to generate wave data. Then, both the wind data and wave data are input
284 into the FVCOM model to calculate the extent of inundation.

285

286 *3.2. Buildings extraction*

287 The deep learning model used in the research is TransUNet (Chen et al., 2021), which was
288 originally proposed for medical images segmentation. TransUNet incorporates transformer in
289 encoder within the architecture of U-shape network, consequently makes use of the advantage of
290 global information extraction while fusing the superficial and deep features. On the mission of
291 building extraction, the target is to segment the building's area precisely. The TransUNet model
292 can effectively identify the boundary between buildings and background, which enables the model
293 to be competent for extracting the buildings in different size and shape.

294   The following is relevant introduction of the structure of the model.

3.2.1. Transformer in TransUNet

296   Transformer was first proposed by Sutskever et al. (2014), which was originally utilized for
297   machine translation. However, as more variants of transform were developed, people found
298   transform also perform well in multiple tasks, such as natural language processing (NLP),
299   computer vision (CV) and automatic speech recognition (ASR).

300   The transformer encoder is composed of L layers of Multi-head Self-Attention (MSA), Layer
301   normalization (LN) and Multi-Layer Perceptron (MLP), the structure is shown in the Fig. 3(a), and
302   the equations of Query-Key-Value (QKV) self-attention and MSA are shown below:

$$\text{Attention}(Q,K,V) = \text{softmax}(\frac{QK^{\mathrm{T}}}{\sqrt{D_k}})V \tag{3.9}$$

$$\text{MultiHeadAttn}(Q,K,V) = \text{Concat}(\text{head}_1, ..., \text{head}_H)\mathbf{W}^O \tag{3.10}$$

$$\text{head}_i = \text{Attention}(QW_i^Q, KW_i^K, VW_i^V) \tag{3.11}$$

303   Where Q, K, V are respectively the Query, Key, Value vector. $\sqrt{D_k}$ is the scaled dot-
304   -product attention. $\mathbf{W}^O$, W_i^Q, W_i^K, W_i^V are respectively the corresponding linear mapping, which
305   convert Q, K, V and the output to the specified dimension.

306   The MSA has a positive effect on helping the model identify the target objects and
307   background, thus the neutral network can learn more information form the target. LN is deemed to
308   stabilize the deep network training, which can prevent unstable gradient, model degradation, etc.
309   The module receives the 2d flatted patches from the image's patches. Due to it is different from
310   CNN or RNN, apart from map the vectorized patches to D-dimensional embedding space,
311   transformer needs to apply additional position encoding for retaining the patch's positional
312   information.

3.2.2. Structure of TransUNet

314   The overall structure of TransUNet is reference to U-Net, which is a U-shaped
315   Encoder-Decoder structure, and the structure diagram is shown in the Fig. 3(b).

316   Encoder: the origin image is put into the CNN part for feature extraction, after the processing
317   of position encoding and flatten, the patches are further put into the transformer module. The
318   transformer module consists of 12 transformer layers. The CNN part is implemented through
319   using resnet50, which include 3 blocks in total, and each block output the hidden feature for skip
320   connection.

321   Decoder: reshape the output sequence from encoder and then cascade up-sampling after
322   transforming the number of channels. During the process, the skip connection is introduced by
323   using the feature map hereinbefore. In the end, the segmentation result is generated.

324   In conclusion, TransUNet is the combination of U-Net and transformer, which is designed to
325   make use of the advantage from both structures. The Global Attention from transformer can
326   contribute to learn the global information, while the skip connection from U-shape network can
327   contribute to get more information from shallow feature map output from CNN, and also CNN
328   performs better in extracting the local information. In this research, buildings images are similar to
329   medical images, with the features like high complexity level, large range of gray values. The skip
330   connection structure can simultaneously acquisition of low-level semantic features and high-level
331   semantic features, and transformer can conduce identify the buildings from background, thus
332   TransUNet achieves a high accuracy in buildings segmentation.
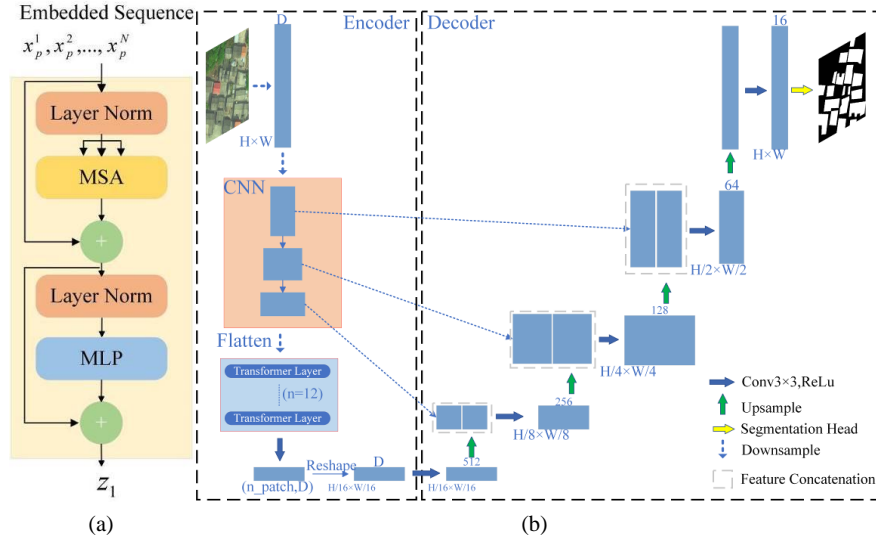
Fig. 3. The overview of TransUNet framework (adapted from (Chen et al., 2021)): (a) Schematic diagram of Transformer layer; (b) Structure diagram of TransUNet

3.3. Building's height acquisition

UAV tilt photography modeling technology can combine control points encryption from massive image data with a small number of ground control points to obtain accurate external orientation elements (Kang et al., 2020). The conducted 3D model reflects the truly condition of the ground, and the data is selected to be in the WGS 1984 coordinate system. The ground resolution is one of the most intuitive and important parameters in tilt photography, and it's also a key factor determining the quality of the 3D modeling. In the process of performing aerial triangulation for tilt-image automation, it is necessary to ensure that the resolution of the different images is as consistent as possible while taking into account the resolution of the side-view image, thus to ensure accuracy and image overlap. Hence, the combinatory analysis of image resolution at tilted viewing angle is required. The tilted image center point, near point and far point resolutions are expressed as follows:

$$\text{GSD}_{\text{top}} = \frac{\delta h \cos \beta_y}{f \cos \left(\alpha_y - \beta_y \right)} \tag{3.12}$$

$$\text{GSD}_{\text{mid}} = \frac{\delta h}{f \cos \alpha_y} \tag{3.13}$$

$$\text{GSD}_{\text{bottom}} = \frac{\delta h \cos \beta_y}{f \cos \left(\alpha_y + \beta_y \right)} \tag{3.14}$$

Where δ is sensor cell size, h is flight height, f refers to the camera focal length, α_y and β_y are respectively dip angle and half the angle of view. Normally, the ground resolution at the center of the tilted and vertical images should be comparable, and the minimum resolution of tilted images should less than three times the resolution of a vertical image.

There are multiple formats available for storing 3D models, including OBJ, STL, FBX,

355 OSGB, etc. In this study, the generated 3D model is saved as OSGB format. OSGB format is
356 originally proposed by Ordnance Survey for storing the geographic spatial data in the British. It
357 combines binary encoding and compression algorithms to improve the data storage and
358 transmission efficiency. Normally, the OSGB data contains information of geographic coordinates,
359 elevation, texture mapping, and geometric shapes, which can be used to GIS application, virtual
360 reality (VR), among others.

361 Digital surface model (DSM) is a digital terrain model that contains more elevation
362 information about trees, buildings, and bridges. Compare to DEM, DSM can reflect the truly
363 surface condition of earth, thus DSM has a wide range of application in city management or forest
364 stewardship. In this research, the UAV data can be transformed to DSM data by using SuperMap
365 software, and the DSM result is shown in Fig. 4(b). After generating the DSM, the elevation of the
366 roof of the building and the corresponding elevation of the ground around the building are
367 extracted by manual selection, then the height of buildings can be calculated by using equation
368 (3.15).

$$DSM_{Roof} - DSM_{Ground} = H \qquad (3.15)$$

369 Where DSM_{Roof} is the DSM value of the building's roof, DSM_{Ground} represents the
370 corresponding DSM value of ground, and H is the result of building's height.
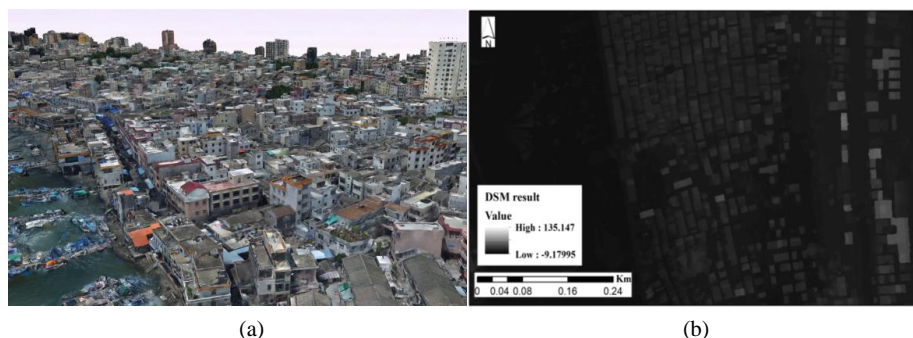
371   (a)   (b)
372 **Fig. 4.** Building's height acquisition: (a) The schematic diagram of UAV tilt photography data; (b)
373   The generated DSM results for Building height data extraction.

374

375 *3.4. Exposure and vulnerability assessment*

376 The process of storm surge risk assessment involves two key components: exposure and
377 vulnerability. The exposure represents the elements exposed to hazardous spaces, while the
378 vulnerability refers to the level of the exposure elements' susceptibility to damage. When doing
379 exposure assessment, the disaster-affected elements can be conducted by overlaying the building
380 footprint data and land cover data with the hazard layer, which is the inundation data in this
381 research. The process can be accomplished using overlay analysis in ArcGIS software.

382 *3.4.1. Adaptation of flood vulnerability functions.*

383 Constructing an empirical stage-damage curve is a commonly used method for conducting
384 vulnerability assessments. However, as is mentioned above, China lacks of the data about flood
385 loss or insurance compensation in flood disasters, as a result, it's not practicable to develop
386 exclusive functions for the study region, so the depth-damage functions developed by Huizinga,
387 Joint Research Center (JRC) (Huizinga et al., 2017) are introduced. The depth-damage functions

388 manifest the loss ratio of the exposure elements in different inundation depth from 0 to 6 m, and
389 the ratio range from 0 to 1, which represents no damage to fully damaged. Besides, JRC also
390 provides the maximum economic losses per square meter for six different exposure element types
391 including residential, industrial, infrastructure, road, agricultural land, and transport. In this study,
392 the original functions and maximum loss data for China region are used, and the economic loss
393 can be calculated by multiplying the loss ratio, the maximum loss, and the disaster-affected area.

394   The building's height is an important factor in flood loss estimation, normally the damage
395 ratio decreases as the number of floors increases (Taramelli et al., 2022). However, the JRC's
396 vulnerability functions do not provide the specific function of each height category. In this case,
397 the depth-damage functions in HAZUS are introduced. HAZUS is first released for earthquakes in
398 1997 by Federal Emergency Management Agency (FEMA), and that's when the HAZUS Flood
399 Model started to be developed (Scawthorn et al., 2006). In 2004, a multi-hazard version called
400 HAZUS-MH was a standardized GIS-based model that included the earthquake, flood, and
401 hurricane models (Nastev and Todorov, 2013). The HAZUS-MH flood model is designed
402 primarily for local and regional hazard planners and emergency managers for developing
403 emergency management plans and mitigation strategies (Tate et al., 2015). However, the
404 depth-damage functions in HAZUS-MH are restricted to regions within America, hence the
405 HAZUS's functions are introduced to adapt JRC's functions.

406   The approach to modifying functions is refered to the method proposed by Dabbeek et al.
407 (2020). In the process, the HAZUS loss ratios of each height category (one-story, two-story, three
408 and more-story) are averaged, which is shown in equation (3.16). Then the contribution of each
409 height category relative to the average loss is calculated as equation (3.17) shows. In the end,
410 multiplying the value obtained in the previous step by JRC's vulnerability functions yields the
411 adapted functions for each height category.

$$\bar{D}_{i(hazus)} = \frac{d_{i,1} + d_{i,2} + d_{i,3+}}{n} \quad i(depth) = \{(0,6)\} \tag{3.16}$$

$$c_{i,h} = \frac{d_{i,h}}{\bar{D}_{i(hazus)}} \tag{3.17}$$

$$d_{i,h(adapted)} = c_{i,h} \times \bar{D}_{i(jrc)} \tag{3.18}$$

412   Where $d_{i,h}$ represents to the loss ratio at the inundation depth i for each height category
413 h. $\bar{D}_i$ is the average loss ratio of all heights.

414

415 *3.4.2. Quantitative risk assessment*

416   The quantitative financial loss estimation is accomplished by overlaying the following data:
417 the inundation simulation result generated by FVCOM and SWAN modeling, the spatial
418 distribution of three types of exposure elements, the depth-damage functions of industrial and
419 commercial elements, and the adapted depth-damage functions for residential elements in three
420 height categories. The process of loss estimation can be shown in the following equation:

$$C = \sum_{i=1}^{i=n} D_{x(i)} f(d_i) A_i \tag{3.19}$$

421   Where C stands for the economic loss estimation result. n represents the total number of
422 exposure elements. $x(i)$ is the type of the i-th element and $D_{x(i)}$ is the maximum loss of the i-th
423 element. d_i is the depth of submergence of the i-th element and $f(d_i)$ is the loss ratio of the i-th

424 element. A_i refers to the area of the i-th element.

425 Comparing to the 984 euros per m² monetary loss of residential buildings in 2010, the

426 monetary loss of infrastructure and agriculture are respectively 12 euros per m² and 0.02 euro per

427 m² according to JRC, only account for 1% or less. Therefore, the monetary loss estimate of

428 infrastructure and agriculture is excluded in the study.

429 In this research, five storm surge scenarios are settled, ten administrative sub-zones are given

430 four different risk levels for each defined typhoon scenario.

431

432 **4. Results and discussions**

433 *4.1. Validation*

434 The performance of coupled FVCOM-SWAN model is evaluated. Four typical typhoons

435 (Vicente, Hato, Mangkhut, Khanun) are selected to validate the coupled model for the study region.

436 The measured data of each typhoon are captured by Department of Natural Resources of Huizhou

437 Bureau. Fig. 5 shows the maximum predicted water level and highest measured water level of the

438 chosen typhoons. Relative error and absolute error are introduced to evaluate the model and Table

439 1 displays the statistical results from Huizhou tidal station. It is seen that the predicted results are

440 in good agreement with the measurements. The statistic result shows that the relative errors of the

441 four typhoons range from 2.1% to 19.8%, and the absolute error varies from 4 cm to 54 cm.

442 Therefore, the coupled FVCOM-SWAN model demonstrates a reliable competence in

443 accomplishing the storm surge simulation task.
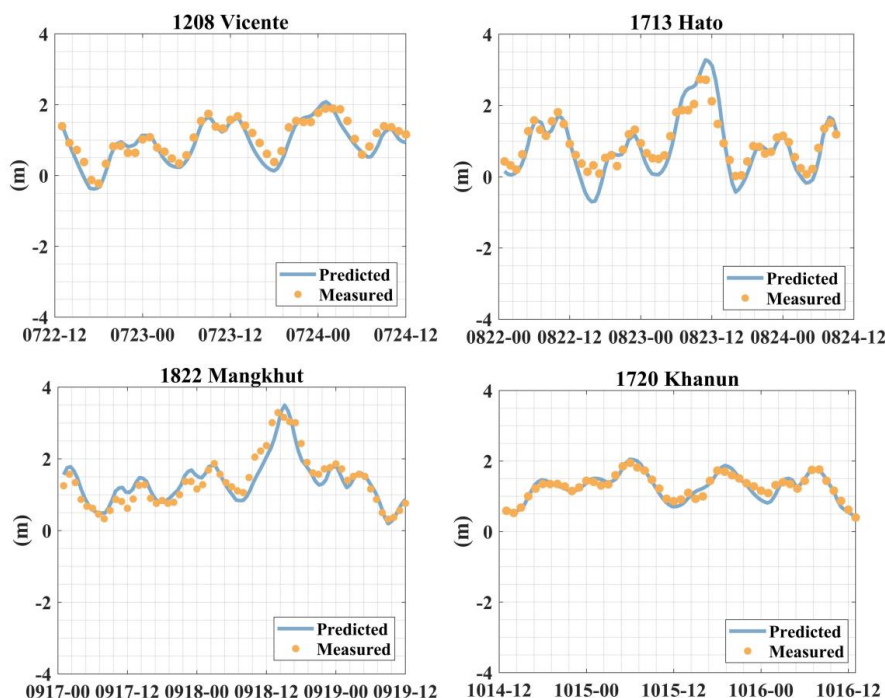
444

445 **Fig. 5.** The predicted water level and highest measured water level recorded by Huizhou tidal

446 station during different typhoon event

447

Natural Hazards
and Earth System
Sciences
Discussions

448 **Table 1.** The Relative error and Absolute error between maximum predicted water levels and highest
449 measured water levels from Huizhou tidal station during different typhoon events

| Typhoon name	Measured data (cm)	Relative error (%)	Absolute error (cm)
Vicente (1208)	189	10.3	19
Hato (1713)	274	19.8	54
Mangkhut (1822)	329	6.5	22
Khanun (1720)	201	2.1	4

450

451 *4.1. Hazard assessment*

452   In the present research, five storm surge inundation scenarios are defined, which represent
453 five different typhoon return periods: 10-year, 20-year, 50-year, 100-year, 1000-year   respectively
454 corresponding to minimum central pressure 940hPa, 930hPa, 920hPa, 910hPa, 880hPa, and the
455 probability of occurrence are 10%, 5%, 2%, 1%, 0.1%. The simulation result is displayed through
456 ArcGIS 10.8 software, and the inundation area and depth simulation results for each scenario is
457 shown in Fig. 6. It is seen that the inundation area is spread over the coastal area in southwest of
458 study area. In particular, for the 1000-year return period scenario, the inundation area exceeds 13
459 km^2 in the study area. Moreover, the presence of Double-Moon Bay leads to the extension of the
460 inundation along the bay, contributing to severe disasters inland.

461   From the point of view of different scenarios, the area of inundation in direct proportion to
462 the typhoon's return period, and the proportion of inundation area increases from 14% to 31% of
463 study area. When the return period is less than 50 years, most of the flooded area is considered to
464 be in a high-level hazard zone, accounting for 75% for a 10-year return period and 67% for a
465 20-year return period, and no zone in very high-level hazard. Basically, the inundation area covers
466 land such as grassland, saline land, and some buildings near the estuary as the area is more
467 susceptible to flooding because of the lower elevation and drainage from the estuary. As the return
468 period goes up to 100 years, 34% and 36% of the flooded area are defined at a high-level hazard
469 and very high-level hazard. When it's 1000-year, the situation worsens with approximately half of
470 the inundation area being considered in very high-level hazard. Typically, the flood extends from
471 the margin of terrene, however, the southernmost region of the investigated area is characterized
472 by a knoll covered by forest vegetation, which serves the dual purpose of water absorption and
473 flood mitigation. In addition, the construction of embankments on both sides of Double-Moon Bay
474 effectively withstands flooding. Nevertheless, because of the presence of the estuary, inadequate
475 water absorption ability of coastal saline soil and the hydrological system, the inundation flows in
476 through the estuary and spreads inland.

477

Natural Hazards
and Earth System
Sciences
Discussions
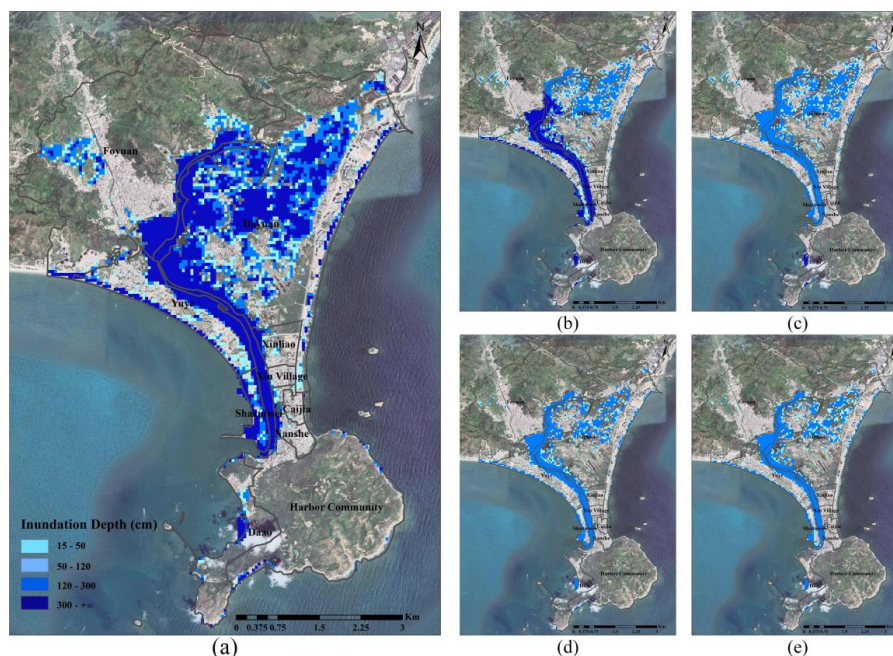
Fig. 6. The storm surge inundation simulation results of different typhoon scenarios. The base map is obtained from © GoogleMaps (map data © 2023 Google).

4.2. Buildings' characters extraction

Buildings are places where human populations gather and distribute, and contain amounts of property, which have great significance in quantitative risk assessment.

4.2.1 TransUNet model training

The dataset construction area is chosen at southwest waterfront region of Renshan Town. The specific location is shown in Fig. 7. The chosen area is a typical area of the Huizhou coastal area. Apart from the seaside bungalows, the area contains some high-rise buildings that are identified as commercial hotels or resorts, while dense residential area is also widely distributed throughout the inland region. In conclusion, the chosen area contains different kinds of buildings with strong representativeness. Since most of the buildings in China coastal towns have the similar characters, the model trained on the representative region has the ability to identify buildings in other regions rapidly.

The labels of the buildings in the area are generated by manually annotation, and the image is cropped to pixels with a size of 256*256. Besides, some of the images without buildings are filtered for preventing the effect of imbalance between the building samples and background samples. In the end, a total of 1200 labeled building dataset is constructed, and the dataset size is deemed sufficient when compared to previous study (Dixit et al., 2021; Ji et al., 2018). The dataset is then divided into a training set and a test set, with the ratio of 8:2. Data enhancement techniques, such as random hue saturation value, random shift scale rotate, flip, and rotate, are implemented during model training to improve the deep learning model's generalization performance and prevent overfitting.

15

503   The training's initial learning rate is set to 1e-5, and the learning rate adjustment strategy for
504   improved training. The batch size is specified as 4, and the number of training epoch is 100. The
505   model is trained on a NVIDIA RTX3060 GPUs.
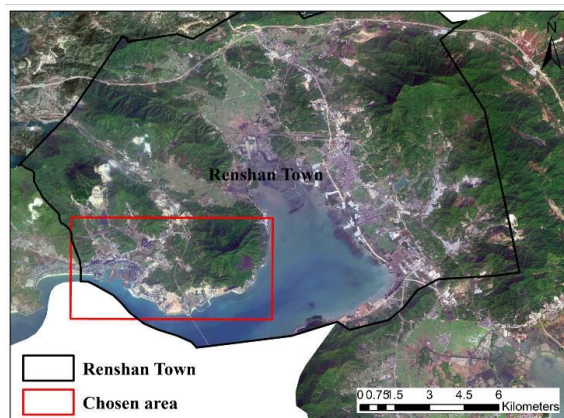
506
507   **Fig. 7.** The chosen area to make the training samples. The base map is obtained from ©
508   GoogleMaps (map data © 2023 Google).
509

510   *4.2.2. Extraction result*

511   Several effective indicators are introduced, including Recall, Precision, F1-score, and mean
512   Intersection-over-Union (mIoU), to evaluate the performance of the deep learning model. Recall is
513   the probability of being predicted as positive among actual positive samples. Precision, on the
514   other hand, is the probability of being actually positive among samples predicted as positive.
515   F1-score serves as an indicator that achieves a balance point between precision and recall,
516   essentially being the harmonic average of precision and recall. mIoU is the mean ratio of the
517   intersection to the union between predicted and true values for each category. True positive (TP)
518   indicates the true samples that are predicted correctly by the model. False positive (FP) indicates
519   the positive samples that the model incorrectly predicted. True negative (TN) and false negative
520   (FN) refer to the number of samples that are correctly and incorrectly predicted as negative by the
521   model. The equations of Recall, Precision, F1-score, and mIoU are as follows:

$$recall = \frac{TP}{TP + FN} \tag{4.1}$$

$$precision = \frac{TP}{TP + FP} \tag{4.2}$$

$$F1 = 2 \times \frac{precision \times recall}{precision + recall} \tag{4.3}$$

$$mIoU = \frac{1}{k+1} \sum_{i=0}^{k} \frac{TP}{TP + FP + FN} \tag{4.4}$$

522   The quantitative evaluation result is shown in Table 2, and the visualization results are
523   illustrated in Fig. 8. As Table 2 shows, the recall score reaches 87% indicating that most of the true
524   building pixels are predicted correctly, and Precision indicates that 82% of all building pixels are
525   correctly detected. Moreover, both the mIoU score and F1-score exceed 80% manifest that the
526   model can balance well between precision and recall. These results reflect the strong performance

16

527 of TransUNet in the building extraction task. After post-processing the result, such as boundary
528 simplification, the building vectorization results can be used for further research in risk assessment.
529 The overall result is shown in Fig. 9.

530 **Table 2.** The statistical accuracy assessment of building footprint extraction

Evaluation metric	
Recall (%)	87.03
Precision (%)	82.04
F1-score (%)	84.46
mIoU (%)	83.38

(a) (b) (c)
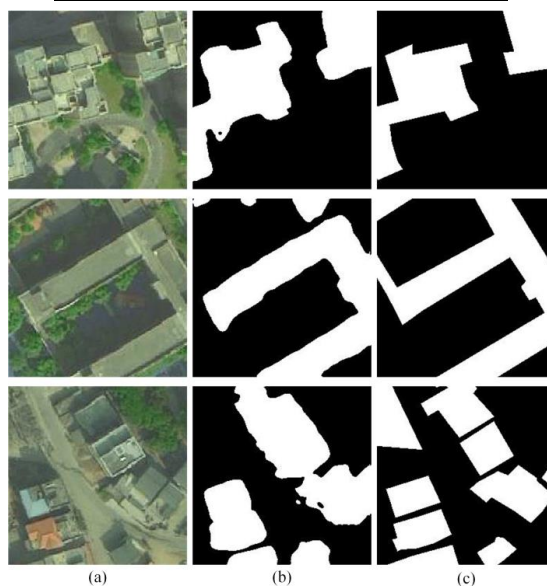
531

532 **Fig. 8.** Building footprint extraction result in study area. (a) Remote sensing images obtained from
533 Jilin-1 satellite (© Chang Guang Satellite technology CO., LTD); (b) Extraction result; (c) Ground
534 truth. The building is marked in white, and the background is marked in black

535

536 *4.2.3. Building height calculation*

537 Through combing two methods mentioned above, the height information is acquired in units
538 of meters. The number of floors is derived by dividing the acquired height information by the
539 specified standard height of 3 meters, according to the China residential design standards. The
540 general condition of building floor is shown in Table 3. Just as mentioned above, the buildings in
541 study area are mainly for residential and commercial use. Since the study area is undeveloped, the
542 high buildings and large mansions is relatively less common, and most of them are built for
543 seaside resort. Instead, buildings with 5 floors or less are the mainstream in study area as respected,
544 which the proportion can reach 76.5%. The building footprint extraction result and building's
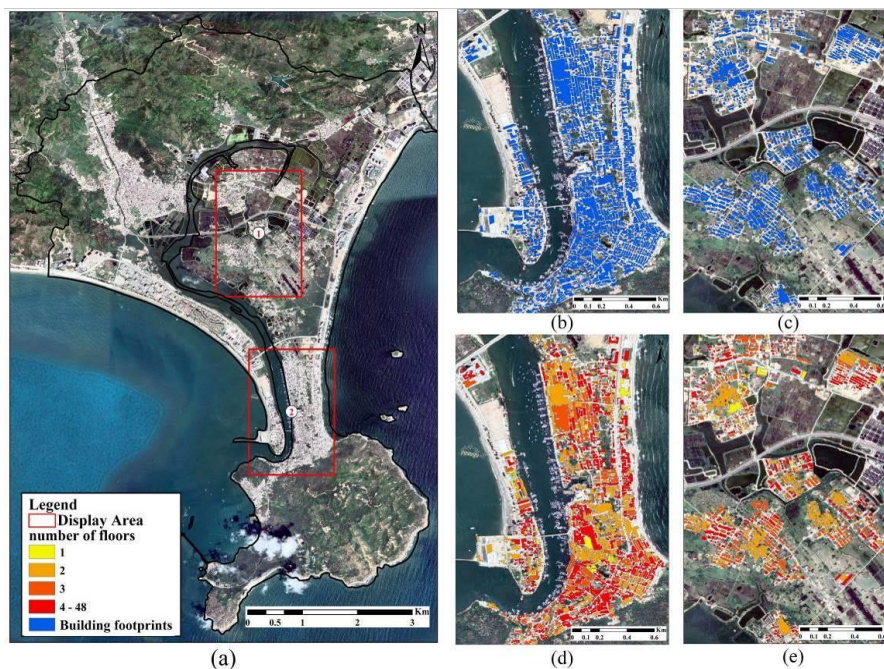545 height information extraction result can be found in Fig. 9.

546 **Table 3.** Statistical results of building height in the study area

Building floor	Area (m²)	Proportion (%)
1-5	17537238.61	76.5

6-10	4996897.08	21.8
11-20	342207.82	1.5
20+	54083.93	0.2

Fig. 9. The building characters extraction result: (a) The schematic of the display area; (b, c) Building footprint result in area 1 and 2; (d, e) Building height result in area 1 and 2. The base map is obtained from © GoogleMaps (map data © 2023 Google).

4.3. qualitative risk assessment

Risk matrix is a risk assessment approach firstly developed by Electronic System Center, which was originally to assess the risk in the life cycle of purchase project (Garvey and Lansdowne, 1998). An additional qualitative risk assessment is conducted using the risk matrix method, incorporating improved land use data to highlight the superiority of building extraction in flood risk assessment.

As is shown in Fig. 10(a), the concentrations of organic town of Dayuan village and Shazuiwei makes it in very high vulnerability level. Under the circumstance of defined 880hPa storm surge scenario, the inundation area spread inland which makes the majority area of Dayuan is regarded as moderate risk, and a fraction of the only very high risk area is distributed in Shazuiwei and north of Dayuan village. In the area of Yuye village, part of the south coastal area is considered in moderate or high risk level. That is mainly because the majority area of Yuye is defined as resort district except for a few areas of tidal flats, which is in high vulnerability. However, after referring to the result of hazard assessment, buildings in the area are not actually inundated, meaning the area should not be at risk level.

Through comparing the Fig. 10(a) and Fig. 10(b), the enhanced land use data in the present

568 research demonstrates a higher ability to recognize vulnerability elements, which the type is
569 buildings in the present research. The two red boxes in the figure highlight the noticeable disparity
570 between the original and current results. The present risk assessment provides more refined risk
571 assessment result compared to the original result, as the previously identified large hazardous
572 areas are replaced with more detailed and smaller zones. This refinement is conducive for
573 government or decision-makers to conduct disaster prevention measures, propose quick guidance
574 for personnel evacuation and organize rescue operations in the event of a disaster.
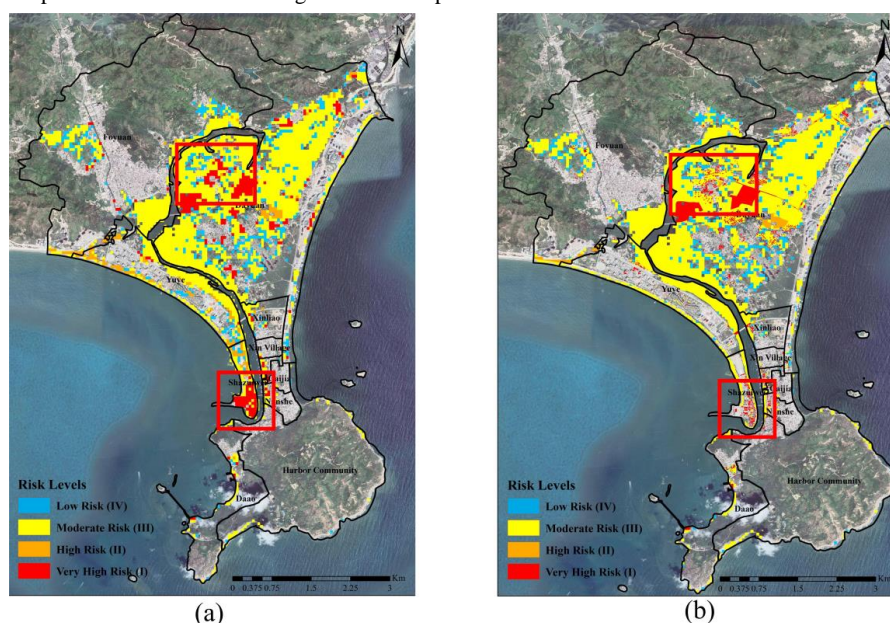
575

576 **Fig. 10.** The risk assessment maps before (a) and after (b) improvement for storm surge scenarios
577 of 1000-year return period. The base map is obtained from © GoogleMaps (map data © 2023
578 Google).

579

580 *4.4. JRC's depth-damage function adaption*

581   Fig. 11 illustrates the damage ratio given flood-depth after adjustment, respectively for one-,
582 two- and more than three-story residential buildings. After adjustment, the damage of one-story
583 residential building function is significantly enhanced, and the loss ratio reach 1 early, which is
584 explicable as 2m-depth flood almost submerges the entire building, resulting in a potential loss of
585 the maximum property value. On the contrary, the loss ratio for multi-story residential building is
586 decreased relative to the original function, it reaches the same level as in the original function
587 when the water depth reaches 5 meters. Furthermore, the function of a two-story residential
588 building is quite similar to that of a building with three or more stories. This can be attributed to
589 the flood's effect on buildings with six meters or less depth being nearly the same, on account of
590 the flood can't overwhelm the entire buildings.

591   Although JRC provides the maximum monetary damages, they are computed for Beijing in
592 2010. However, there is a substantial difference in the level of development between Beijing and
593 the study area. For better matching the financial level in study area, adjustment can be achieved

594 based on scaling the maximum monetary damage value with the GDP ratio according to Huizinga
595 (2007). Based on the 2010 GDP of Beijing of 14113558 million yuan and the GDP of Huizhou of
596 172995 million yuan, the maximum monetary damage is adjusted by equal proportions. Besides,
597 the price level also needs to be adjusted to the 2022 price level. According to the World Bank, the
598 Chinese consumer price index (CPI) has changed from 100 in 2010 to 131.9 in 2022, the tendency
599 of variation and the adjusted maximum monetary damages are shown in Fig. 12.

600

601 (a)   (b)
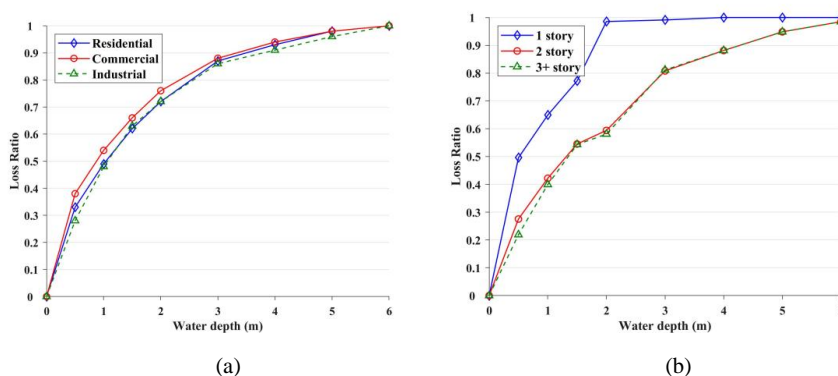
602 **Fig. 11.** (a) The depth-damage function proposed by JRC; (b) The adapted depth-damage function
603 for residential buildings in different floors

604

605 (a)   (b)
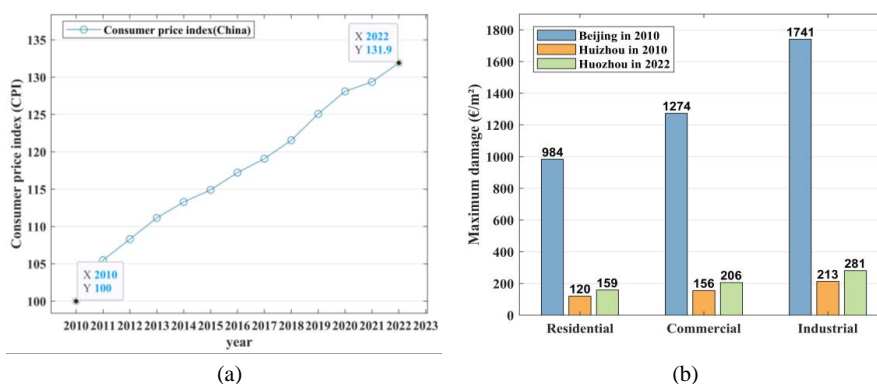
606 **Fig. 12.** (a) The variation trend of Consumer price index released by World Bank; (b) The
607 maximum monetary damage per m² for each type of exposed elements in China (in 2010 and in
608 2022).

609

610 *4.5. Quantitative risk assessment*

611   Loss assessments of five storm surge scenarios are computed for return periods of 10, 20, 50,
612 100, and 1000 years, through employing the method in section 3. The estimate monetary damage
613 is summarized in Table 4.

614   The statistical data in Table 4 demonstrate an increase in the affected area and total economic
615 loss with an increasing return period. Comparing to the total affected area of 131533.12 m² and
616 the total economic losses of 9330517.49 euros with the 10-year return period, the

617 corresponding estimate result with 1000-year return period is 917437.99 m^2 and 68364923.25
618 euros, which is both approximately seven times higher. This indicates a proportional
619 relationship between the extent of regional impairment and the return period of a typhoon.
620 Although the impacted area for the 20-year and 50-year return periods exhibits relative
621 proximity as the different is 24118.26 m^2, there is still a significant disparity in economic
622 losses. According to the inundation result above, that's because the inundation area of two
623 return period is nearly the same except for the slight difference in the northeast of the study
624 region, but the flood depth of 50-year intensified, which causes more monetary damage. In
625 terms of inundated building types, in case that study area is characterized as a tourism and
626 fish breeding area, the proportion of economic losses in industrial is relatively low. The losses
627 of residential buildings and commercial buildings is comparatively close, up until the severity
628 of storm surge reach 50-year return period. At this point, the losses experienced by residential
629 buildings exceed those incurred by commercial buildings by more than double. The fact can
630 be explained by the commercial buildings area mainly constructed by the seaside for better
631 turnover therefore both type of waterfront buildings is impacted. However, as the severity of
632 the typhoon worsens, more residential settlements inland are flooded, resulting in a swift
633 increase in economic losses for residential buildings.

634 **Table 4.** The statistic result of the quantitative risk assessment for five defined typhoon scenarios.

| Scenario	Elements	Area (m^2)	Economic losses (€)	Total losses (€)	Probability	Risk (€)
10-year (940hPa)	Residential	94847.11	4910882.27	9330517.49	0.1	933051.75
	Commercial	36163.62	4281840.09			
	Industrial	522.39	137795.12			
20-year (930hPa)	Residential	216010.31	7872861.19	13665211.91	0.05	683260.60
	Commercial	55423.59	5602828.01			
	Industrial	522.39	189522.71			
50-year (920hPa)	Residential	237572.35	16509796.15	24607011.73	0.02	492140.23
	Commercial	57979.81	7775321.70			
	Industrial	522.39	321893.88			
100-year (910hPa)	Residential	291759.48	19857901.69	28446797.47	0.01	284467.97
	Commercial	75123.51	8194736.70			
	Industrial	833.39	394159.08			
1000-year (880hPa)	Residential	762570.09	49295364.67	68364923.25	0.001	68364.92
	Commercial	149457.01	17907591.59			
	Industrial	5410.89	1161967.00			

635

636 Based on the economic losses estimation result for five storm surge scenarios, through using
637 zonal statistics method on the data of administrative sub-zones in the study area, the quantitative
638 risk assessment is conducted. The economic losses and spatial distribution of storm surge risk for
639 ten sub-zones in five different scenarios are shown in Fig. 13. The zonation statistics result map of
640 each sub-zone is defined at four different risk levels (very high, high, moderate, low). The
641 classification of risk levels is obtained by categorizing all zonal statistic result based on quantiles.
642 As is shown in Fig. 13, Dayuan village is considered in very high risk for every defined
643 typhoon scenario. Through analyzing the geographical characteristics of the study area, it can be

644 found that although Dayuan is a relatively inland village, it's surrounded by the watercourse of the
645 estuary of Double-Moon Bay. Due to the existence of flood control dam, both side of the bay offer
646 a measure of protective effectiveness, which result in the water level rises in inland watercourse,
647 and further causes flooding of residential buildings in Dayuan village, leading to massive financial
648 losses. In contrast, Foyuan village is also a village with a relatively large area, the risk is at
649 moderate level for 10, 20-year return period, and the level escalates to high for 50, 100-year return
650 period and reaches very high in 1000-year. Considering the presence of the knoll, the spread of
651 inundation is hindered. However, as typhoon becomes more severe, the inundation hit the western
652 buildings in the region, which led to the phenomenon of progressively escalating risk level. In
653 terms of those villages with relatively smaller sizes, due to the protection of dam, Xinliao village,
654 Xin village, Caijia village all are defined in relatively low risk level, although the regions with a
655 high density of buildings. Shazuiwei and Yuye village in different return period are considered in
656 different risk level, the cause of this phenomenon might be that apart from the higher density of
657 buildings, the buildings in Shazuiwei are distributed in coastal area, combing the impact of
658 inundation of both sides as it's located at the outermost part of the gulf. Consequently, the risk
659 level in Shazuiwei remains consistently high as opposed to gradually increasing like in Yuye
660 village. Although they are located at the outermost part of the study area, the quantitative risk level
661 of Daao village and Harbor community is gradually increasing for different return period, but it's
662 not as serious as the other village, which can be explained that these locations exhibit elevated
663 topography.

664 The quantitative risk assessment and zonal risk maps can assist the government or decision-
665 makers in recognizing the specific economic losses of each sub-zones, so it's helpful to identify
666 the areas that are more susceptible to experiencing significant losses, which allows them to
667 develop disaster prevention measures, for example constructing disaster prevention facilities,
668 budget allocation for disaster prevention and planning evacuation strategies. Besides, establishing
669 the quantitative risk for different typhoon periods can enhance the decision makers understanding
670 of the potential vulnerability in each sub-zone, and facilitates the implementation of appropriate
671 preventive and disaster relief measures facing different typhoon intensity.
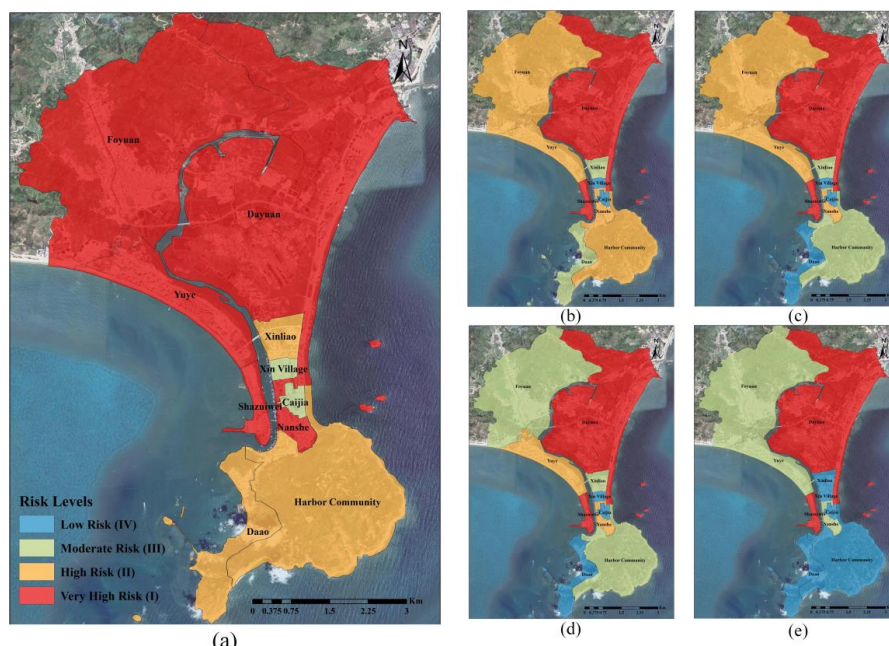
Fig. 13. The zonation maps of the quantitative risk assessment for five defined typhoon scenarios: return period (a) 1000-year, (b): 100-year, (c): 50-year, (d): 20-year, (e): 10-year. The base map is obtained from © GoogleMaps (map data © 2023 Google).

5. Conclusions

These years, the academic research on storm surge risk assessment has been greatly developed due to climate change and financial growth in coastal area. However, the quantitative risk assessment is inexecutable in the undeveloped area since on account of the lacks of building characters and damage assessment data. Target at the question above, the purpose of this paper is to propose a method for conducting refined storm surge risk assessment quantitatively based on deep learning and GIS techniques. Firstly, the reliable coupled FVCOM-SWAN model is utilized to simulate five defined storm surge scenarios. Facing the challenge of the absence of data, a deep learning method TransUNet is applied to extract the building footprint data for refined extraction of exposed elements, and buildings' height data is acquired through UAV. To compensate for that the available depth-damage functions do not taking building's height into account, the functions are adjusted for buildings with different floor and consequently to perform more refined monetary losses calculations in five defined scenarios. Eventually, the quantitative risk assessment and zonation maps of the study area are generated base on GIS techniques

The quantitative risk assessment result of the study region shows that on account of the existence of estuary and the gathering of buildings, Dayuan village presents the high-risk level in all defined typhoon scenario, and the economic loss risk is large. The flood control dam provides protection of Xinliao village, Xin village, Caijia village, which prevents the regions suffering large economic losses as the typhoon return period is 10-year and 20-year. However, the storm surges, under the typhoon scenarios that the return period is greater than 50-year, can overwhelm the existed dikes, and both the commercial buildings and residential buildings suffer heavy economic

Natural Hazards
and Earth System
Sciences
Open Access
EGU
Discussions

697 losses. Therefore, it's necessary to make land use planning and adjustment especially in Dayuan
698 and Shazuiwei as they are under very high-risk level to prevent the impact and losses caused by
699 storm surges. Besides, the regions that is nearest to the sea doesn't mean they suffer greater
700 potential economic loss, as the risk level of Daao village and Harbor community are considered at
701 a relatively low level because of the topographical characteristics and the distribution of buildings.

702 The study provides a framework for refined quantitative storm surge risk assessment
703 targeting the problem of acquiring exposure elements and the establishing multi-variable empirical
704 depth-damage functions, as a consequence of missing data in underdeveloped regions. The
705 generated results can help the decision-makers to identify the areas that are susceptible to
706 experiencing significant losses efficiently, and help the respective authorities with disaster
707 prevention, future land use planning and material deployment. Furthermore, it is important to
708 remark that, the methodology of this paper has general applicability, since the applied models are
709 publicly available. Thus, there is also potential for further application. For example, the
710 framework can be applied in other coastal areas in China, as they have similar characters, which
711 also means there is a possibility to utilize in larger scales. Furthermore, the framework can also be
712 performed in other types of disasters, such as flood, earthquake, and mudslide. Consequently, the
713 proposed methodology demonstrates an extensive relevance to the scientific community.

714 There is still room for improvement in this study. The current study relied on manual labeling
715 in terms of distinguishing between functional areas to conduct risk assessment. In the future study,
716 efforts will be made to distinguish the types of exposure elements in a more objective way, based
717 on diverse data sources such as social media Point Of Interest (POI). Additionally, exploring the
718 activity patterns of the population through multiple sources of data including taxi trajectories and
719 smart cards can contribute to the consideration of population risks in different storm surge
720 scenarios, thereby prompting more comprehensive risk assessments.

721

Data availability.

723 Remote sensing images are obtained from Chang Guang Jilin-1 satellite. The dataset of wind field
724 is generated by ERA5 and Holland method. The Administrative Boundary data is obtained from
725 National geographic information public service platform. The datasets can be obtained from
726 https://dx.doi.org/10.6084/m9.figshare.24586605 (Yu, 2023). DEM data and UAV data are
727 obtained from Department of Natural Resources of Huizhou Bureau, data sets are not publicly
728 available due to the policy of the Natural Resources of Huizhou Bureau.

729

730 Competing interests. The authors declare that they have no conflict of interest.

731

Authorship contributions.

733 **Lichen Yu**: Investigation, Methodology, Data Curation, Visualization, Formal analysis, Writing -
734 Original Draft. **Shining Huang**: Investigation, Data Source, Data Curation, Visualization, Formal
735 analysis. **Hao Qin**: Conceptualization, Methodology, Validation, Supervision, Writing - Original
736 Draft, Project administration, Funding acquisition. **Wei Wei**: Validation, Data Curation,
737 Visualization. **Lin Mu**: Conceptualization, Supervision, Project administration, Funding
738 acquisition.

739

Acknowledgement

745

References

748 Adnan, M. S. G., Abdullah, A. Y. M., Dewan, A., and Hall, J. W.: The effects of changing land use and
749 flood hazard on poverty in coastal Bangladesh, Land Use Policy, 99, 104868, 2020.

750 Armenakis, C. and Nirupama, N.: Estimating spatial disaster risk in urban environments, Geomatics,
751 natural hazards and risk, 4, 289-298, 2013.

752 Booij, N., Holthuijsen, L. H., and Ris, R. C.: The" SWAN" wave model for shallow water, in, 668-676,
753 1996.

754 Chen, C., Liu, H., and Beardsley, R. C.: An unstructured grid, finite-volume, three-dimensional,
755 primitive equations ocean model: application to coastal ocean and estuaries, Journal of atmospheric and
756 oceanic technology, 20, 159-186, 2003.

757 Chen, D. and Gao, G. X.: Probabilistic graphical fusion of LiDAR, GPS, and 3D building maps for
758 urban UAV navigation, Navigation, 66, 151-168, 2019.

759 Chen, J., Lu, Y., Yu, Q., Luo, X., Adeli, E., Wang, Y., Lu, L., Yuille, A. L., and Zhou, Y.: Transunet:
760 Transformers make strong encoders for medical image segmentation, arXiv preprint arXiv:2102.04306,
761 2021.

762 China Marine disaster bulletin: Historical Marine disasters in China,available at:
763 http://www.mnr.gov.cn/sj/sjfw/hy/gbgg/zghyzhgb/, last access: 12 November 2023.

764 Dabbeek, J., Silva, V., Galasso, C., and Smith, A.: Probabilistic earthquake and flood loss assessment in
765 the Middle East, International Journal of Disaster Risk Reduction, 49, 101662, 2020.

766 de Moel, H. and Aerts, J. C. J. H.: Effect of uncertainty in land use, damage models and inundation
767 depth on flood damage estimates, Natural Hazards, 58, 407-425, 2011.

768 Dixit, M., Chaurasia, K., and Kumar Mishra, V.: Dilated-ResUnet: A novel deep learning architecture
769 for building extraction from medium resolution multi-spectral satellite imagery, Expert Systems with
770 Applications, 184, 115530, 2021.

771 Fang, J., Wahl, T., Fang, J., Sun, X., Kong, F., and Liu, M.: Compound flood potential from storm surge
772 and heavy precipitation in coastal China: dependence, drivers, and impacts, Hydrology and Earth
773 System Sciences, 2021.

774 Gacu, J. G., Monjardin, C. E. F., de Jesus, K. L. M., and Senoro, D. B.: GIS-Based Risk Assessment of
775 Structure Attributes in Flood Zones of Odiongan, Romblon, Philippines, Buildings, 13, 506, 2023.

776 Garvey, P. R. and Lansdowne, Z. F.: Risk matrix: an approach for identifying, assessing, and ranking
777 program risks, Air Force Journal of Logistics, 22, 18-21, 1998.

778 Grahn, T. and Nyberg, R.: Damage assessment of lake floods: Insured damage to private property
779 during two lake floods in Sweden 2000/2001, International journal of disaster risk reduction, 10,
780 305-314, 2014.

781 Granger, K.: Quantifying storm tide risk in Cairns, Natural Hazards, 30, 165-185, 2003.

782 Hess, T. M. and Morris, J.: Estimating the value of flood alleviation on agricultural grassland,
783 Agricultural Water Management, 15, 141-153, 1988.

784 Hu, K., Meselhe, E., Rhode, R., Snider, N., and Renfro, A.: The Impact of Levee Openings on Storm

785   Surge: A Numerical Analysis in Coastal Louisiana, Applied Sciences, 12, 10884, 2022.

786   Huizinga, H. J.: Flood damage functions for EU member states, HKV Consultants, Implemented in the
787   framework of the contract, 382442-F382441SC, 2007.

788   Huizinga, J., De Moel, H., and Szewczyk, W.: Global flood depth-damage functions: Methodology and
789   the database with guidelines,   2017.

790   Ji, S., Wei, S., and Lu, M.: Fully convolutional networks for multisource building extraction from an
791   open aerial and satellite imagery data set, IEEE Transactions on geoscience and remote sensing, 57,
792   574-586, 2018.

793   Ji, T., Li, G., Liu, Y., Liu, R., and Zhu, Y.: Spatiotemporal Features of Storm Surge Activity and Its
794   Response to Climate Change in the Southeastern Coastal Area of China in the Past 60 years, Journal of
795   Geophysical Research: Atmospheres, 126, 2020.

796   Kang, C. L., Cheng, Y., Wang, F., Zong, M. M., Luo, J., and Lei, J. Y.: THE APPLICATION OF UAV
797   OBLIQUE PHOTOGRAMMETRY IN SMART TOURISM: A CASE STUDY OF LONGJI
798   TERRACED SCENIC SPOT IN GUANGXI PROVINCE, The International Archives of the
799   Photogrammetry, Remote Sensing and Spatial Information Sciences, XLII-3/W10, 575-580, 2020.

800   Kreibich, H., Seifert, I., Merz, B., and Thieken, A. H.: Development of FLEMOcs – a new model for
801   the estimation of flood losses in the commercial sector, Hydrological Sciences Journal, 55, 1302-1314,
802   2010.

803   Kron, W.: Flood risk= hazard• values• vulnerability, Water international, 30, 58-68, 2005.

804   Lee, J.: The economic aftermath of Hurricanes Harvey and Irma: The role of federal aid, International
805   journal of disaster risk reduction, 61, 102301, 2021.

806   Liu, W.-C. and Huang, W.-C.: Investigating typhoon-induced storm surge and waves in the coast of
807   Taiwan using an integrally-coupled tide-surge-wave model, Ocean Engineering, 212, 107571, 2020.

808   Liu, Y., Li, Z., Wei, B., Li, X., and Fu, B.: Seismic vulnerability assessment at urban scale using data
809   mining and GIScience technology: application to Urumqi (China), Geomatics, Natural Hazards and
810   Risk, 10, 958-985, 2019.

811   Liu, Y., So, E., Li, Z., Su, G., Gross, L., Li, X., Qi, W., Yang, F., Fu, B., and Yalikun, A.:
812   Scenario-based seismic vulnerability and hazard analyses to help direct disaster risk reduction in rural
813   Weinan, China, International Journal of Disaster Risk Reduction, 48, 101577, 2020.

814   Lyddon, C. E., Brown, J. M., Leonardi, N., Saulter, A., and Plater, A. J.: Quantification of the
815   Uncertainty in Coastal Storm Hazard Predictions Due to Wave-Current Interaction and Wind Forcing,
816   Geophysical Research Letters, 46, 14576-14585, 2019.

817   Malekinezhad, H., Sepehri, M., Pham, Q. B., Hosseini, S. Z., Meshram, S. G., Vojtek, M., and
818   Vojteková, J.: Application of entropy weighting method for urban flood hazard mapping, Acta
819   Geophysica, 69, 841-854, 2021.

820   Masson, D.: A case study of wave–current interaction in a strong tidal current, Journal of physical
821   oceanography, 26, 359-372, 1996.

822   McGranahan, G., Balk, D., and Anderson, B.: The rising tide: assessing the risks of climate change and
823   human settlements in low elevation coastal zones, Environment and urbanization, 19, 17-37, 2007.

824   McPherson, M.: Responding to Typhoon Haiyan in the Philippines, Western Pacific Surveillance and
825   Response Journal, 6, 1-4, 2015.

826   Merz, B., Kreibich, H., and Lall, U.: Multi-variate flood damage assessment: a tree-based data-mining
827   approach, Natural Hazards and Earth System Sciences, 13, 53-64, 2013.

828   Merz, B., Thieken, A. H., and Gocht, M.: Flood risk mapping at the local scale: concepts and

Natural Hazards
and Earth System
Sciences
Discussions

EGU
Open Access

829 challenges, Flood risk management in Europe: innovation in policy and practice, 231-251, 2007.

830 Mharzi Alaoui, H., Radoine, H., Chenal, J., Hajji, H., and Yakubu, H.: Deep building footprint
831 extraction for urban risk assessment–Remote sensing and Deep learning based approach, The
832 International Archives of the Photogrammetry, Remote Sensing and Spatial Information Sciences, 48,
833 83-86, 2022.

834 Nastev, M. and Todorov, N.: Hazus: A standardized methodology for flood risk assessment in Canada,
835 Canadian Water Resources Journal, 38, 223-231, 2013.

836 Paprotny, D., Kreibich, H., Morales-Nápoles, O., Castellarin, A., Carisi, F., and Schröter, K.: Exposure
837 and vulnerability estimation for modelling flood losses to commercial assets in Europe, Science of The
838 Total Environment, 737, 140011, 2020.

839 Pathan, A. I., Girish Agnihotri, P., Said, S., and Patel, D.: AHP and TOPSIS based flood risk
840 assessment- a case study of the Navsari City, Gujarat, India, Environmental Monitoring and
841 Assessment, 194, 2022.

842 Rafiei-Sardooi, E., Azareh, A., Choubin, B., Mosavi, A. H., and Clague, J. J.: Evaluating urban flood
843 risk using hybrid method of TOPSIS and machine learning, International Journal of Disaster Risk
844 Reduction, 66, 102614, 2021.

845 Ramkar, P. and Yadav, S. M.: Flood risk index in data-scarce river basins using the AHP and GIS
846 approach, Natural Hazards, 109, 1119-1140, 2021.

847 Rousell, A. and Zipf, A.: Towards a Landmark-Based Pedestrian Navigation Service Using OSM Data,
848 ISPRS international journal of geo-information, 6, 64, 2017.

849 Scawthorn, C., Blais, N., Seligson, H., Tate, E., Mifflin, E., Thomas, W., Murphy, J., and Jones, C.:
850 HAZUS-MH flood loss estimation methodology. I: Overview and flood hazard characterization,
851 Natural Hazards Review, 7, 60-71, 2006.

852 Seto, K. C., Fragkias, M., Güneralp, B., and Reilly, M. K.: A meta-analysis of global urban land
853 expansion, PloS one, 6, e23777, 2011.

854 Shi, X., Tan, J., Guo, Z., and Liu, Q.: A review of risk assessment of storm surge disaster, Advances in
855 Earth Science, 28, 866, 2013.

856 Smith, D. I.: Flood damage estimation - A review of urban stage-damage curves and loss functions,
857 Water S. A., 20, 231-238, 1994.

858 Sutskever, I., Vinyals, O., and Le, Q. V.: Sequence to sequence learning with neural networks,
859 Advances in neural information processing systems, 27, 2014.

860 Tang, J., Wang, L., and Yao, Z.: Analyzing urban sprawl spatial fragmentation using multi-temporal
861 satellite images, GIScience & Remote Sensing, 43, 218-232, 2006.

862 Taramelli, A., Righini, M., Valentini, E., Alfieri, L., Gatti, I., and Gabellani, S.: Building-scale flood
863 loss estimation through vulnerability pattern characterization: application to an urban flood in Milan,
864 Italy, Natural Hazards and Earth System Sciences, 22, 3543-3569, 2022.

865 Tate, E., Munoz, C., and Suchan, J.: Uncertainty and sensitivity analysis of the HAZUS-MH flood
866 model, Natural Hazards Review, 16, 04014030, 2015.

867 Thieken, A. H., Olschewski, A., Kreibich, H., Kobsch, S., and Merz, B.: Development and evaluation
868 of FLEMOps : a new Flood Loss Estimation MOdel for the private sector, Southampton, 315-324,

869 Vijayan, L., Huang, W., Yin, K., Ozguven, E., Burns, S., and Ghorbanzadeh, M.: Evaluation of
870 parametric wind models for more accurate modeling of storm surge: a case study of Hurricane Michael,
871 Natural Hazards, 106, 2003-2024, 2021.

872 Wang, N., Hou, Y., Mo, D., and Li, J.: Hazard assessment of storm surges and concomitant waves in

873   Shandong Peninsula based on long-term numerical simulations, Ocean & Coastal Management, 213,
874   105888, 2021a.

875   Wang, S., Mu, L., Yao, Z., Gao, J., Zhao, E., and Wang, L.: Assessing and zoning of typhoon storm
876   surge risk with a geographic information system (GIS) technique: a case study of the coastal area of
877   Huizhou, Natural Hazards and Earth System Sciences, 21, 439-462, 2021b.

878   Wu, J., Ye, M., Wang, X., and Koks, E.: Building Asset Value Mapping in Support of Flood Risk
879   Assessments: A Case Study of Shanghai, China,   2019.

880   Yang, Z., Shao, W., Ding, Y., Shi, J., and Ji, Q.: Wave Simulation by the SWAN Model and FVCOM
881   Considering the Sea-Water Level around the Zhoushan Islands, Journal of Marine Science and
882   Engineering, 8, 783, 2020.

883   Yazdi, J. and Salehi Neyshabouri, S. A. A.: Optimal design of flood-control multi-reservoir system on a
884   watershed scale, Natural hazards (Dordrecht), 63, 629-646, 2012.

885   Yu, L: NHESS_dataset, 10.6084/m9.figshare.24586605.v2,   2023.

886   Zhai, G., Fukuzono, T., and Ikeda, S.: MODELING FLOOD DAMAGE: CASE OF TOKAI FLOOD
887   20001, Journal of the American Water Resources Association, 41, 77-92, 2005.

888   Zhang, Z., Chen, C., Song, Z., Zhang, D., Hu, D., and Guo, F.: A FVCOM study of the potential coastal
889   flooding in apponagansett bay and clarks cove, Dartmouth Town (MA), Natural Hazards, 103,
890   2787-2809, 2020.

891   Zhou, G., Song, C., Simmers, J., and Cheng, P.: Urban 3D GIS from LiDAR and digital aerial images,
892   Computers & geosciences, 30, 345-353, 2004.

893   Zhu, T., Ke, S., Li, W., Chen, J., Yun, Y., and Ren, H.: WRF-CFD/CSD analytical method of
894   hydroelastic responses of ultra-large floating body on maritime airport under typhoon-wave-current
895   coupling effect, Ocean Engineering, 261, 112022, 2022.

896